

This is the accepted manuscript made available via CHORUS. The article has been published as:

Active microrheology of smectic membranes

Zhiyuan Qi, Kyle Ferguson, Yancey Sechrest, Tobin Munsat, Cheol Soo Park, Matthew A. Glaser, Joseph E. Maclennan, Noel A. Clark, Tatiana Kuriabova, and Thomas R. Powers

Phys. Rev. E **95**, 022702 — Published 22 February 2017

DOI: [10.1103/PhysRevE.95.022702](https://doi.org/10.1103/PhysRevE.95.022702)

Active Microrheology of Smectic Membranes

Zhiyuan Qi^{1, 2}, Kyle Ferguson^{1, 2}, Yancey Sechrest¹, Tobin Munsat¹, Cheol Soo Park^{1, 2}, Matthew A. Glaser^{1, 2}, Joseph E. MacLennan^{1, 2}, and Noel A. Clark^{1, 2}
*Department of Physics¹ and Soft Materials Research Center²,
University of Colorado, Boulder, Colorado, 80309, USA*

Tatiana Kuriabova
Department of Physics, California Polytechnic State University, San Luis Obispo, California, 93407, USA

Thomas R. Powers
*School of Engineering and Department of Physics,
Brown University, Providence, Rhode Island, 02912, USA*
(Dated: January 26, 2017)

Thin, fluid membranes embedded in a bulk fluid of different viscosity are of fundamental interest as experimental realizations of quasi-two-dimensional fluids and as models of biological membranes. We have probed the hydrodynamics of thin, fluid membranes by active microrheology using small tracer particles to observe the highly anisotropic flow fields generated around a rigid, oscillating post inserted into a freely suspended smectic liquid crystal film that is surrounded by air. In general, at distances more than a few Saffman lengths from the meniscus around the post, the measured velocities are larger than the flow computed by modeling a moving, disk-like inclusion of finite extent by superposing Levine/MacKintosh response functions for point-like inclusions in a viscous membrane. The observed discrepancy is attributed to additional coupling of the film with the air below the film that is displaced directly by the shaft of the moving post.

PACS numbers: 83.80.Xz, 47.57.Lj, 68.15.+e, 83.60.Bc

I. INTRODUCTION

Experiments involving the in-plane motion of inclusions confined to a two-dimensional (2D) viscous liquid surrounded above and below by a three-dimensional (3D) fluid with lower viscosity (referred to hereafter as the *embedding fluid* [1]) are useful for understanding the diffusion, aggregation and transport of proteins, plasma, and lipid molecules [2–4] in biological systems. Stimulated by experiments in biomembranes [5, 6], Saffman and Delbrück (SD) [7, 8] developed a general theory describing the diffusion of inclusions with radius much smaller than the membrane’s Saffman length $\ell_S = h\eta/(2\eta')$ (where h is the thickness of the membrane, η is the viscosity of the membrane, and η' the viscosity of the embedding fluid), a characteristic hydrodynamic distance over which the membrane around the inclusion does not exchange momentum with the embedding fluid [9]. By solving the Navier-Stokes equations numerically, Heringa, Wiegels, and van Beckum [10, 11] computed the mobility of inclusions of arbitrary size in embedded membranes, obtaining results that were subsequently confirmed by a more general, analytical model developed by Hughes, Pailthorpe, and White (HPW) [12]. The HPW description has been extensively verified in passive microrheology experiments on several membrane/embedding fluid systems [13–15].

By virtue of their lamellar nature, freely suspended films of smectic liquid crystal (LC) are quantized locally in thickness to a certain number of layers [16], stabilizing hydrodynamic parameters such as density and viscos-

ity to an extent comparable to that of 3D fluids. Many previous studies of membrane/embedding fluid systems have focused on understanding the behavior of inclusions undergoing Brownian diffusion but there have been few direct experimental investigations of the hydrodynamic properties of 2D fluid membranes using active microrheology. Eremin et al. [17] observed the flow field generated by an inclusion (a small bead) moving down an inclined smectic A film under the force of gravity using tracer particles. These experiments were carried out using very thick films, where the effect of the embedding fluid is negligible and the hydrodynamics are those of a (bounded) 2D fluid. A detailed analysis of the flow fields generated by actively driven inclusions in smectic films (including comparison to theory) has, however, not yet been performed.

Thermal diffusion of inclusions such as smectic islands and liquid droplets is associated with local, positional fluctuations that are stochastic in nature and do not result in movements large enough to generate long-range flow fields. Manipulation of such inclusions using optical tweezers [18, 19], although able to cause large amplitude motion, tends to heat up the film locally and change the thermodynamic properties of the LC material. Here we describe experiments in which a thin, cylindrical metal post inserted into nanometer-thick, smectic A films is actively driven in order to generate large-scale flow in the membrane in the low-Reynolds-number regime.

II. EXPERIMENT

We measured the 2D flow field generated by the moving post by analyzing the motion of small tracer particles in the film. The flow fields were extracted from digital video using velocimetric software and compared with the generalized Levine/MacKintosh theory summarized in the following section.

The post was a gold-coated tungsten wire $6\text{ }\mu\text{m}$ in radius and approximately 1 cm long. The lower end of the wire was attached to a thicker, steel rod connected to a leaf spring that was made to oscillate parallel to the film.

We explored two different methods of exciting the post mechanically. When the post assembly was driven directly using a piezoelectric actuator, the high driving voltages required would sometimes cause the tracer particles in the film to be repelled from the vicinity of the post. A better technique, in which the field generated by an electromagnet couples to a small, permanent magnet attached to the base of the post (see Fig. 1), eliminated this problem and avoided flow artifacts associated with electroconvection in the film.

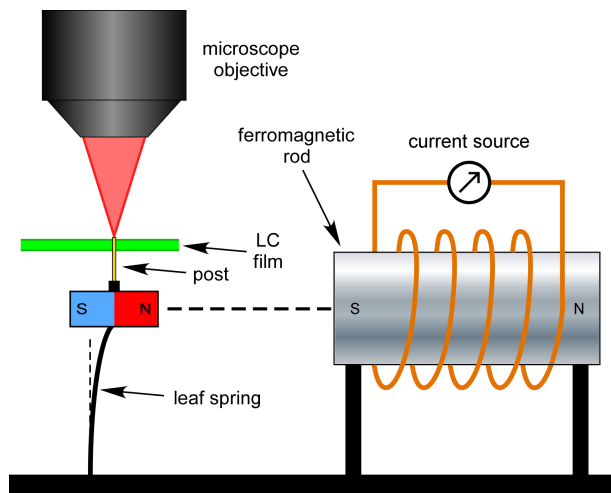


FIG. 1. (Color online) Oscillating post assembly for generating flow in smectic films. A thin metal post mounted on top of a small permanent magnet is carefully raised until it penetrates the liquid crystal film above it. The magnet is attached to a leaf spring that allows it to move from side to side. By varying the current in the coil of a nearby electromagnet, the post can be displaced laterally at a controlled rate. The resulting flow induced in the film is monitored using reflected light video microscopy.

Films were drawn by spreading the liquid crystal material 8CB (4'-n-octyl-4'-cyanobiphenyl, Sigma-Aldrich) across an aperture in a glass cover slip. The flow with the post far from any boundaries was measured in circular films 1 cm in diameter, while boundary effects were studied near the long edge of a $20\text{ mm} \times 4\text{ mm}$ rectangular film. 8CB is in the smectic A liquid crystal phase (a layered, 2D fluid) at room temperature and has viscosity

$\eta = 0.052\text{ Pa}\cdot\text{s}$ [20]. The films were typically two to six molecular layers thick, each layer having a thickness of 3.17 nm [21]. The film thickness was determined by comparing the reflectivities of the film and a piece of black glass [22]. The films are bounded above and below by air, with a viscosity of $\eta' = 1.827 \times 10^{-5}\text{ Pa}\cdot\text{s}$ [23]. The Saffman lengths ℓ_S in our experiments were $13.534\text{ }\mu\text{m}$ for $N = 3$ layers and $22.556\text{ }\mu\text{m}$ for $N = 5$ layers.

Once a film was drawn, it was placed in a chamber that was filled with smoke. Ash particles that settled onto the film served as tracer particles that allowed the flow field to be visualized in subsequent experiments. The ash particles are small and their effect on the hydrodynamic behavior of the film can be neglected. The tip of the post was wetted with a small amount of the LC so that it would not rupture the film on contact, after which it was raised just enough to pierce the membrane. Within a few minutes, a meniscus formed an annulus around the post, resulting in an inclusion with an effective radius many times larger than the post itself. Here we present data from experiments where the inclusion radii were between 33.5 and $110\text{ }\mu\text{m}$, in all cases larger than the corresponding Saffman length.

The post was then displaced laterally through approximately $50\text{ }\mu\text{m}$ using a 2 Hz triangle wave, the post velocity being constant during each half cycle. This generated flow in the film in the low-Reynolds-number regime ($\text{Re} \approx 10^{-5}$), which was observed using reflected light microscopy and captured using a Phantom v12.1 video camera with 1080×720 pixel resolution at 60 frames per second. The video clips were then decomposed into images for further analysis. The velocimetric method used to determine the flow fields is described in Appendix A.

III. THEORY

In 2002, Levine and MacKintosh (LM) [24] found the response function for a viscoelastic membrane embedded in a bulk fluid, describing the velocity at a point \mathbf{x} induced by a point force \mathbf{f} applied at location \mathbf{x}' in the membrane by

$$v_\alpha(\mathbf{x}) = G_{\alpha\beta}(\mathbf{x} - \mathbf{x}')f_\beta(\mathbf{x}'). \quad (1)$$

If \hat{x} is the unit vector pointing from \mathbf{x}' to \mathbf{x} , then the response function may be decomposed into parallel and perpendicular components as

$$G_{\alpha\beta}(\mathbf{x}) = G_{\parallel}(|\mathbf{x}|)\hat{x}_\alpha\hat{x}_\beta + G_{\perp}(|\mathbf{x}|)[\delta_{\alpha\beta} - \hat{x}_\alpha\hat{x}_\beta], \quad (2)$$

where

$$G_{\parallel}(z) = \frac{1}{4\pi\eta h} \left[\frac{\pi}{z} H_1(z) - \frac{2}{z^2} - \frac{\pi}{2} [Y_0(z) + Y_2(z)] \right] \quad (3)$$

and

$$G_{\perp}(z) = \frac{1}{4\pi\eta h} \left[\pi H_0(z) - \frac{\pi}{z} H_1(z) + \frac{2}{z^2} - \frac{\pi}{2} [Y_0(z) - Y_2(z)] \right] \quad (4)$$

Here $z = |\mathbf{x}|/\ell_S$ is the non-dimensionalized distance between the location of the point force and the point of observation of the velocity field, H_ν are Struve functions, and Y_ν are Bessel functions of the second kind.

We have applied the LM results to the special case of finding the flow field around inclusions in a purely viscous membrane of thickness h and viscosity η embedded in a bulk fluid of viscosity η' . Theoretical flow fields around an inclusion are calculated by modeling the inclusion by a ring of point forces and exploiting the linearity of Stokes flow to represent the resulting flow as a superposition of LM response functions [25, 26]. This approach also allows us to consider the effects of proximity to a stationary linear boundary: for a circular inclusion near a linear boundary the flow is

$$v_{\alpha}(\mathbf{x}) = \int d\phi f_{\beta}(\phi) G_{\alpha\beta}(\mathbf{x} - \mathbf{x}'(\phi)) + \int dy g_{\beta}(y) G_{\alpha\beta}(\mathbf{x} - \mathbf{x}'(y)), \quad (5)$$

where $f_{\beta}(\phi)$ is the force per unit angle at the point $\mathbf{x}'(\phi)$ on the boundary of the inclusion, and $g_{\beta}(y)$ is the force per unit length at the point $\mathbf{x}'(y)$ on the linear boundary of the membrane. These forces can be determined by assuming no-slip boundary conditions $v_{k\alpha} = V_{k\alpha}$ and $v_{k\alpha} = 0$ on the circular and linear boundaries respectively and then solving Eq. (5) numerically.

Prasad, Koehler, and Weeks [27] studied experimentally the motion of beads much smaller than the Saffman length embedded in a fluid membrane and verified the validity of the LM approach. By observing the mutual diffusion of pairs of circular inclusions of arbitrary size in freely suspended films of smectic A liquid crystal, which are fluid-like in the plane of the membrane, Qi et al. [25] found that the radial mutual mobilities of identical inclusions are independent of their size but that the angular coupling becomes strongly size-dependent when their radius exceeds the Saffman length. It was shown further that these observations are described well for arbitrary inclusion separations by the extended Levine/MacKintosh theory described above.

IV. RESULTS AND DISCUSSION

The flow induced in the LC film near the moving inclusion was measured under a variety of experimental conditions. In particular, we examined the effects on the flow fields of inclusion size and of proximity to a straight boundary.

We consider first an inclusion with effective radius $110 \mu\text{m}$ (8.1 times the Saffman length of an $N = 3$ -layer smectic A 8CB film) located near the middle of

a circular film, far from any boundaries, driven back and forth in order to generate in-plane flow. A sample microscope image of the film in reflected light is shown in Fig. 2(a). The instantaneous velocity of the post (shown in yellow, here and in every figure) is along $+\hat{y}$. The bright spots are tiny ash particles, each of which is surrounded by a narrow meniscus of liquid crystal material. The slightly irregular appearance of the inclusion is an illumination artefact caused by the uneven tip of the wire. Since the meniscus around the post (outlined in green) is much thicker than the smectic film, the interior of the inclusion is effectively hydrodynamically isolated from the surrounding film and may be considered essentially rigid [28]. An example of the measured flow velocity field is given in Fig. 2(b), the green ring showing the outline of the moving inclusion. The general appearance of the 2D flow field predicted by LM theory for a disk-shaped inclusion of the same diameter as the meniscus surrounding the post, shown in Fig. 2(c), suggests overall qualitative agreement with the experimental observation. We shall see below, however, that there are important differences in the detailed behavior revealed by the measured 1D flow velocity profiles that we propose arise from the motion of the air around the shaft of the post immediately below the film, which couples to the membrane and gives an important additional contribution to the flow field in the film.

The flow field is anisotropic, as expected, with the flow falling off more quickly beside the inclusion (along x) than fore and aft (along y), as is evident from the flow velocity profiles along these directions shown in Figs. 3(a) and (b). The velocity in this case, where the inclusion is far from any boundaries, falls off monotonically with distance in all directions and has the same sign everywhere, indicating that there is no recirculation of the flow field within the field of view near the inclusion. The measured velocity profiles are plotted as red symbols with error bars. The black curve shows the spatial variation of velocity predicted by LM theory for a disk-like inclusion moving in the film. The blue curve shows the estimated velocity profile of the air around the post some distance below the film. Here and in all figures, we plot the magnitude of the velocity v scaled by v_0 , the speed of the post. The dashed curve is a combination of the LM results with a fraction of the air flow chosen to give rough, qualitative agreement with the experimental observations far from the inclusion.

In general, the experimentally observed velocities when the post is near the middle of the film are higher and decay more slowly with distance than predicted for an idealized, disk-like inclusion. We ascribe this to additional coupling between the shaft of the post and the layer of air directly beneath the film. Since the shaft of the post is on the order of a centimeter in length, it has a large length/diameter ratio so that, beginning a short distance below the film, the airflow near the post approximates that around an infinite cylinder moving laterally in a bounded region defined by the film holder (see Ap-

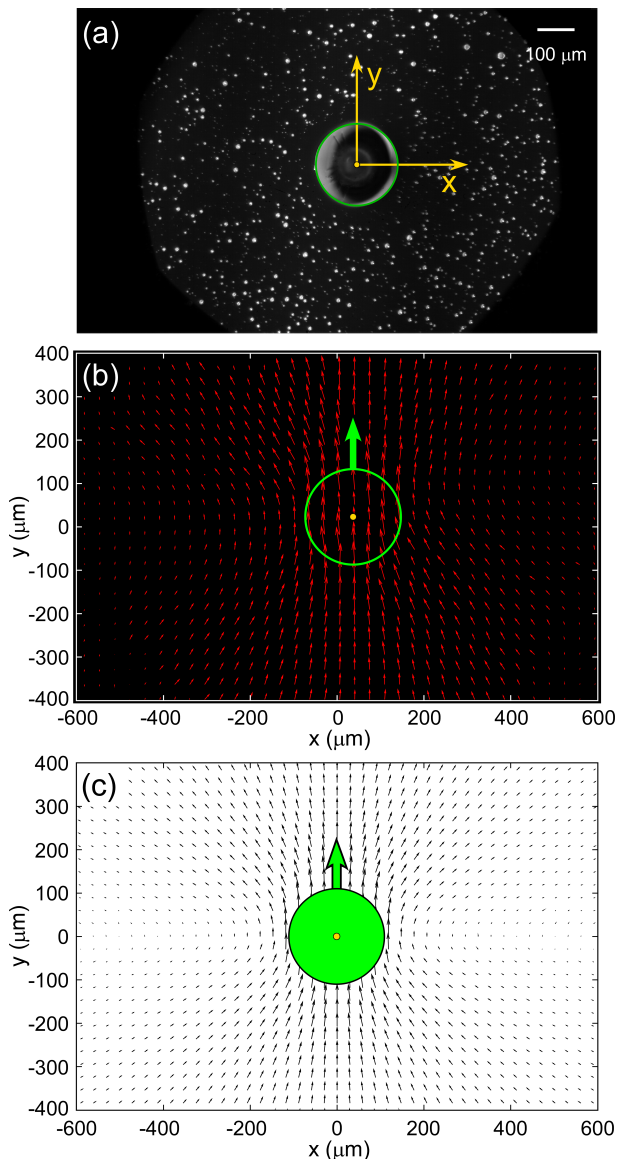


FIG. 2. (Color online) Flow generated by a big inclusion around a moving post located far from any boundaries in an $N = 3$ -layer 8CB film. The location of the post is shown in yellow and the inclusion in green. (a) Reflected microscope image of the inclusion (radius $a = 110 \mu\text{m}$), which is moving along y . The white dots are ash particles embedded in the film. (b) Experimental flow field obtained by analyzing trajectories of tracer particles. The instantaneous velocity of the post, also measured by velocimetry, is $v_0 = 143 \mu\text{m}/\text{sec}$. (c) Model 2D flow field predicted by generalized LM theory. While similar in overall appearance, the model agrees only qualitatively with experiment.

pendix B for details of this calculation). The 2D air flow around such an idealized post is depicted in Fig. 4. Since the viscosity of air is much smaller than that of LC, this velocity field decays much more slowly than flow in the membrane. We postulate that the moving layer of air near the film couples to the LC, effectively boosting the

flow in the film and leading to a more gradual decay of the flow velocity with distance than predicted for a moving, disk-like inclusion alone.

A complete, three-dimensional hydrodynamic treatment of this experimental geometry is theoretically challenging and beyond the scope of this paper. Since the Stokes equations are linear, however, we have as a first approximation explored a model in which a constant fraction of the estimated air flow around the post is added to the LM prediction at that radius. This is not proposed as a rigorous model (it does not satisfy the boundary conditions near the inclusion meniscus, after all). Nevertheless, the combined velocity profiles obtained by fitting the experimental data at distances more than $5\ell_S$ from the edge of the inclusion, shown as dashed curves in Figs. 3 and 5, do approximate the measured velocities more closely than LM theory alone, supporting the notion that the observed deviations from the LM model for an ideal, disk-like inclusion in a quasi-2D membrane result from coupling to airflow generated by the post beneath the film. We note that the discrepancy between the experimental measurements and LM theory is consistently larger for inclusions with smaller radius. This is principally a reflection of the behavior of the LM model, which predicts membrane velocity fields that decay more rapidly with decreasing inclusion size. In addition, the magnitude of the computed air flow from the post, which falls off relatively slowly, is larger at the outer radius of a smaller inclusion than at the outer edge of a bigger inclusion (about 16% higher along the y -direction and 50% along x in the examples shown in Figs. 5 and 3). These effects combine to make the contribution of the air more important the smaller the inclusion.

In order to explore the effects on the flow of the proximity of the inclusion to the film boundary, we measured the flow field in the film when the post was located near the long edge of a rectangular film. The flow field when the inclusion is moving parallel to the boundary is shown in Fig. 6(a). The corresponding LM flow field calculated for a disk-like inclusion (assuming no-slip boundary conditions at both the disk and the meniscus at the film edge), shown in Fig. 6(b), is similar to the experiment. However, in the transverse direction, while the LM model predicts that there should be recirculation of the flow field on both sides of the inclusion, experimentally this is only clearly observed on the side of the inclusion further from the boundary. The measured flow velocity profiles parallel and perpendicular to the inclusion motion plotted in Fig. 7 show that the velocity attains a minimum value between the inclusion and the meniscus at the edge of the film but does not become negative, increasing instead to a small but finite value at the film edge. This suggests that the no-slip boundary condition assumed in the model may not perfectly reflect conditions at the edge of the film. We note that symmetric, circulatory flow has been observed previously in smectic A films, around a bead moving under gravity down the middle of a tilted, thick rectangular film with dimensions comparable to or

smaller than the Saffman length as described above [17].

Finally, the flow field measured around an inclusion of intermediate size moving normal to a straight film boundary nearby is shown in Fig. 8(a). In this case, there is significant recirculation, with vortex-like flow observed on both sides of the post, in agreement with the model predictions shown in Fig. 8(b). The velocity decays rapidly to zero on approaching the boundary and falls off more slowly in the opposite direction. The measured velocity profiles along and perpendicular to the direction of post motion are shown in Figs. 9(a) and (b), along with the LM model predictions.

In general, LM theory alone appears to predict the flow fields induced in the film much better when the moving post is near the boundary than when it is in the center of the film, with the LM model profiles in Figs. 7(a) and 9(a) closely approximating the experimental data. This result indicates that near the film boundaries, the air flow induced by the post is greatly reduced and does not boost the flow in the film significantly.

V. CONCLUSION

We have described active microrheology experiments on a two-dimensional, embedded viscous fluid, in which the flow field around a rigid, moving post inserted into a thin film of smectic liquid crystal surrounded by air is measured by analyzing the motion of small tracer particles in the film. The observed flow fields around the meniscus surrounding the post are compared with predictions based on generalized Levine/MacKintosh theory for the flow around a disk-like inclusion in a 2D fluid membrane. When the moving inclusion is far from the film boundaries, the measured velocity field decays more slowly in all directions than predicted by the model, an effect ascribed to additional coupling of the film to air around the shaft of the post. When the inclusion is near the film boundary, LM theory alone reproduces the observed flow fields quite well, suggesting that near the boundaries any air flow contributed directly by the post is negligible.

This work was supported by NASA Grant NNX-13AQ81G, by the Soft Materials Research Center under NSF MRSEC Grants DMR-0820579 and DMR-1420736, by Department of Energy Grant DE-FG02-08ER54995, and by NSF Grant CBET-0854108.

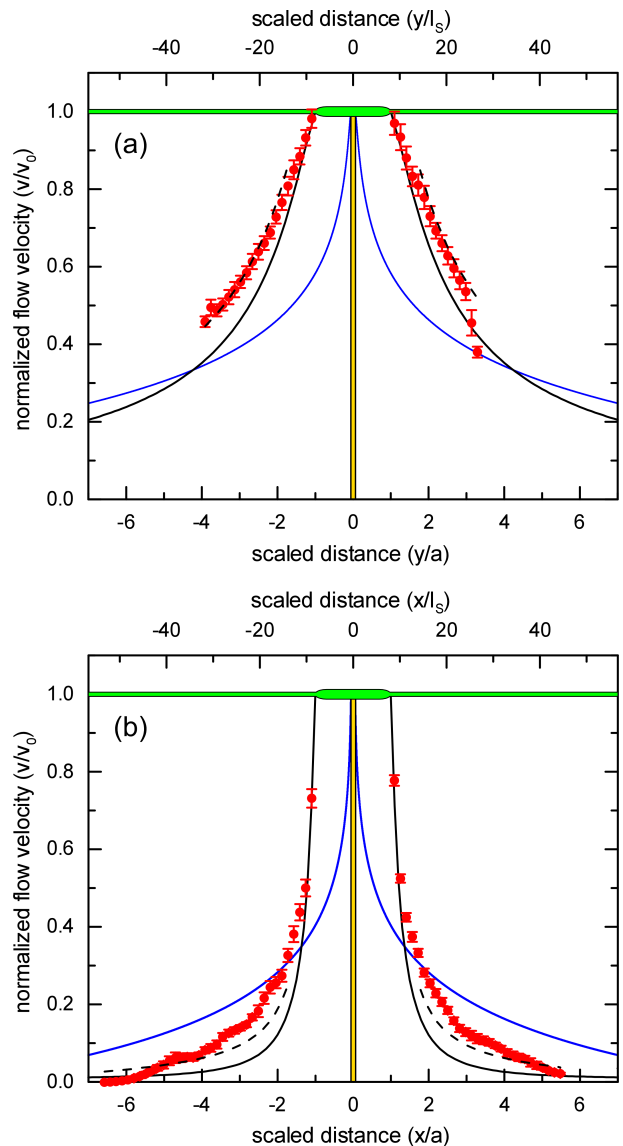


FIG. 3. (Color online) Normalized flow velocity profiles measured (a) along and (b) perpendicular to the direction of post motion for the big inclusion in an $N = 3$ -layer 8CB film shown in Fig. 2. The post (radius $b = 6 \mu\text{m}$) is shown in yellow, and the smectic film and the inclusion (radius $a = 110 \mu\text{m}$, or $8.1 \ell_S$) embedded in it in green. The black curves are LM model predictions for a disk-like inclusion, while the blue curves show the flow velocity profiles of air generated by an infinitely long, moving post with no-slip boundary conditions. Away from the inclusion boundary, the experimental data lie above the LM curves, suggesting that flow in the film is boosted by air flow generated by the shaft of the post. The dashed curve shows the flow profile obtained by adding 26% of this air flow to the LM prediction. The velocities are scaled by the instantaneous post velocity v_0 and distances both by the inclusion radius a and the Saffman length ℓ_S . The velocity measurements were averaged over 10 different oscillation cycles, with the error bars showing the standard deviation of the mean.

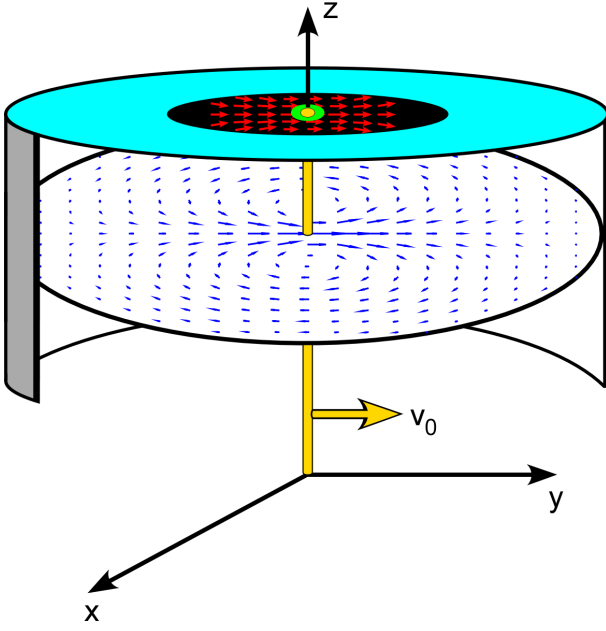


FIG. 4. (Color online) Computed flow around a moving post inserted into a fluid liquid crystal film. The post (yellow) moves along the y direction with velocity v_0 . The nominal flow field in the film around the inclusion (green) is estimated by integrating LM point response functions for a disk-like inclusion, while the quasi-2D flow in the air is found by solving the 2D Stokes equations around an infinite cylinder, assuming no-slip conditions at the boundaries defined by the film holder. The air couples to the flow in the membrane to give a slower decay of the film velocity than predicted by LM theory alone.

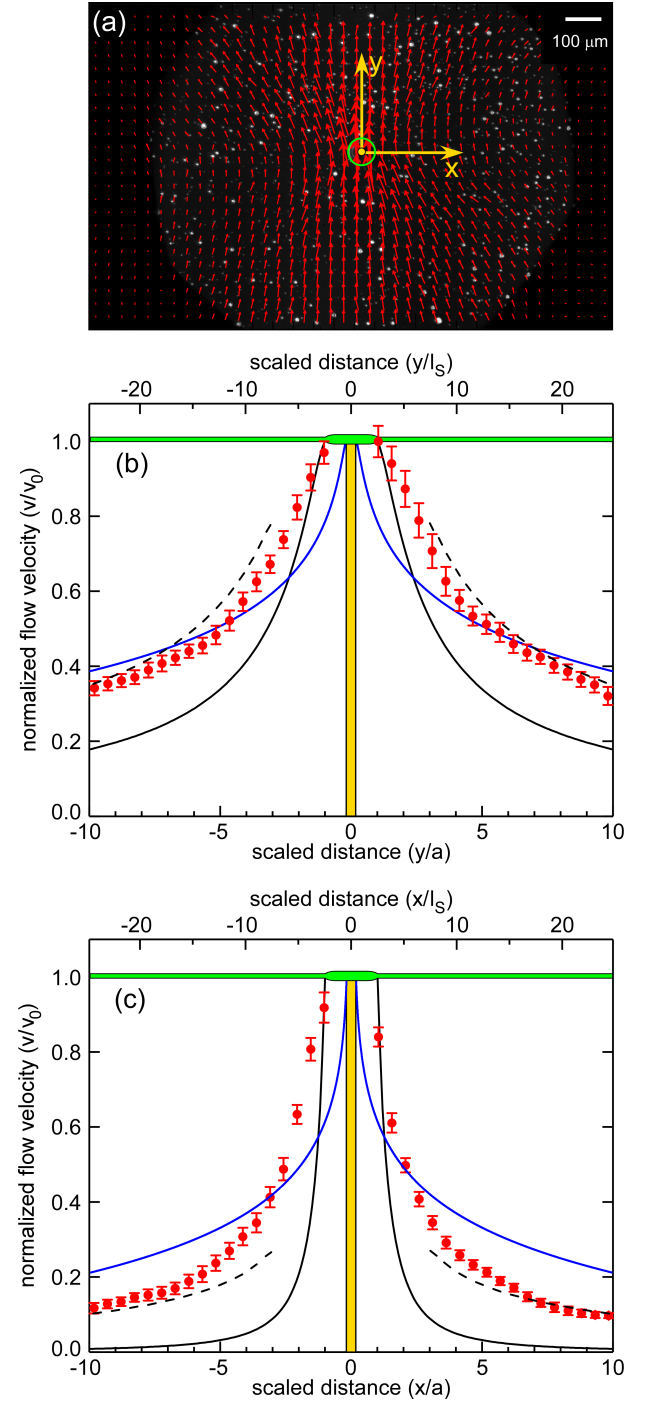


FIG. 5. (Color online) Flow field generated by a small inclusion (radius $a = 33.5 \mu\text{m}$, or $2.58 \ell_S$) formed around a thin, moving post inserted near the middle of an $N = 3$ -layer 8CB film. (a) Measured flow field superimposed on the corresponding microscopic image, showing the locations of the post (yellow) and inclusion (green). Flow velocity profiles were extracted along the directions (b) parallel and (c) transverse to the inclusion motion. The deviation of experimental data from LM theory (black curve) is larger here than for the bigger inclusion shown in Fig. 3. The velocity profile in air around an infinite, cylindrical post is shown in blue. The dashed curve shows the flow profile obtained by adding 45% of this air flow to the LM prediction.

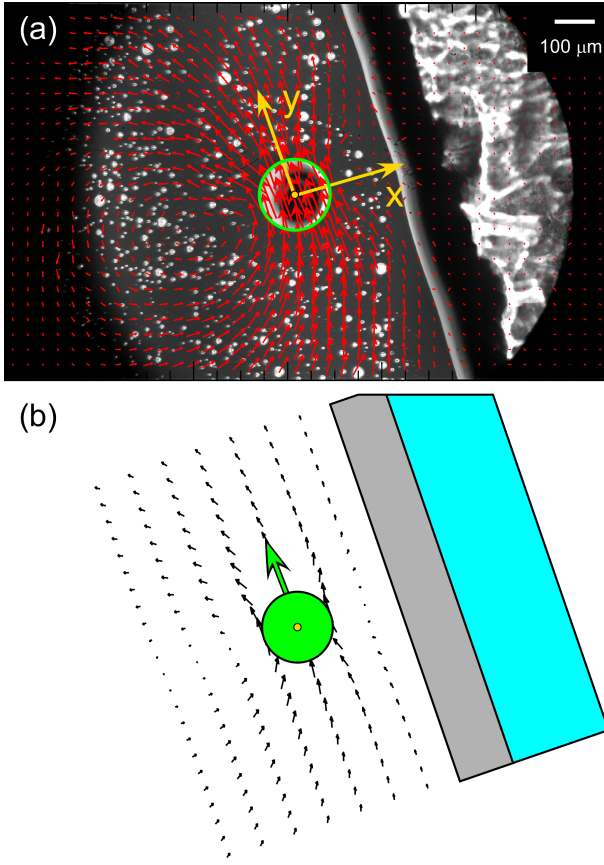


FIG. 6. (Color online) Flow field generated by an inclusion of intermediate size (radius $a = 80.5 \mu\text{m}$, or $3.58 \ell_S$) moving parallel to a straight film boundary. (a) Observed flow field superimposed on the reflected microscopic image of an $N = 5$ -layer film. The center of the post is located $232 \mu\text{m}$ from the edge of the film and is moving along y . (b) Model flow field associated with a disk-like inclusion moving under the same conditions as in (a). LM theory predicts that recirculation of the flow field should be observed on both sides of the inclusion but in the experiment this is only clearly visible on the side further from the boundary. The meniscus at the edge of the film is shown as gray and the glass film holder as blue.

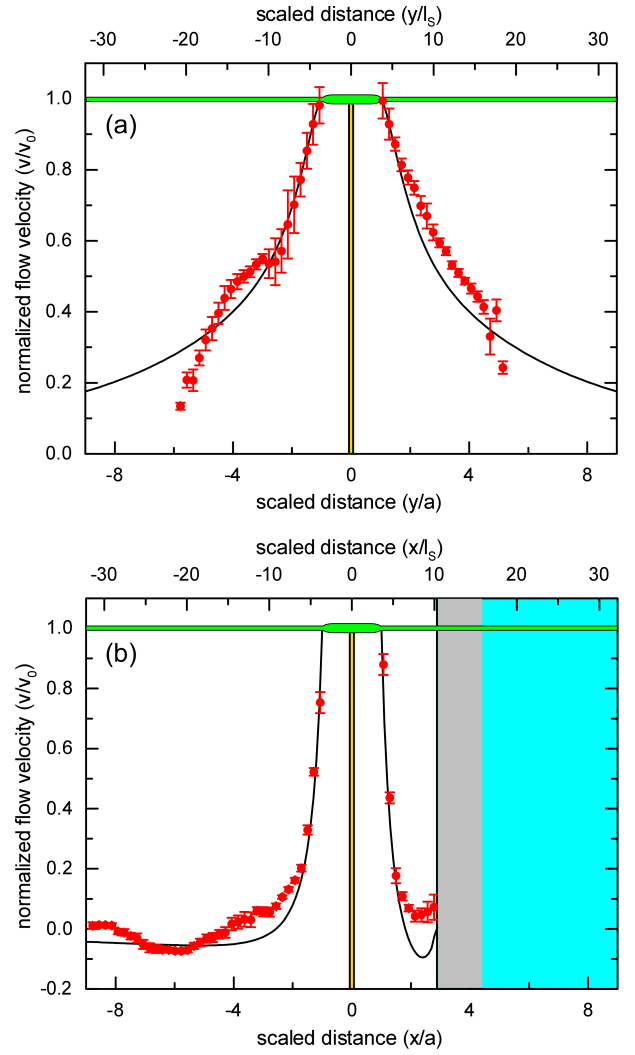


FIG. 7. (Color online) Normalized film flow velocity profiles near the inclusion moving parallel to the film boundary shown in Fig. 6, measured (a) along y and (b) along x . The black curves are LM model predictions for a disk-like inclusion. Negative velocities indicate flow with a component opposite the post motion, i.e., flow reversal.

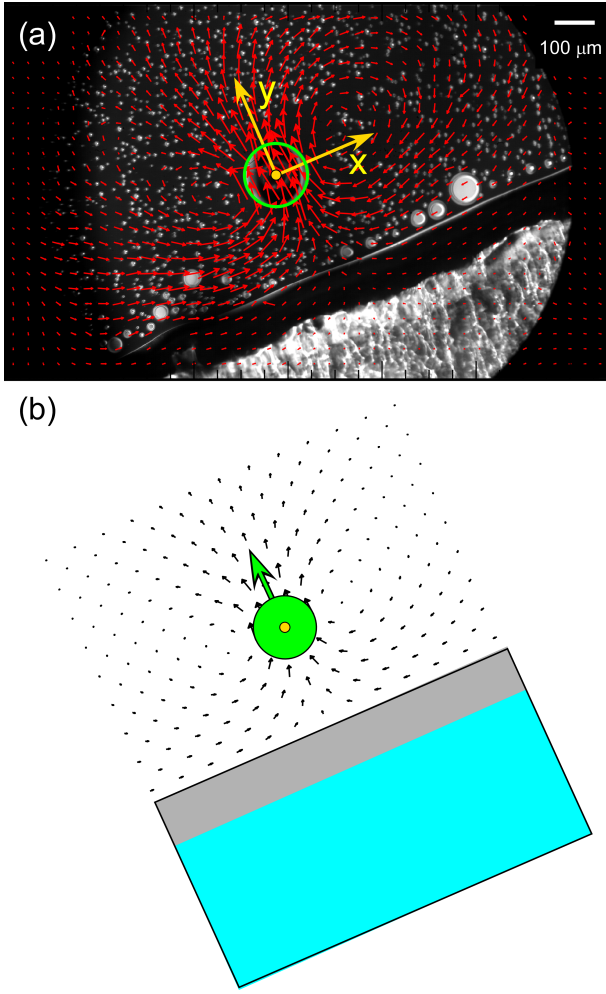


FIG. 8. (Color online) Flow field generated by an inclusion of intermediate size (radius $a = 75.5 \mu\text{m}$, or $5.59 \ell_S$) moving perpendicular to a straight film boundary. (a) Observed flow field superimposed on the reflected microscopic image of an $N = 3$ -layer film. The center of the inclusion is located $258 \mu\text{m}$ from the film boundary and it is moving along y . (b) Model flow field associated with a disk-like inclusion moving under the same conditions as in (a). The proximity to a no-slip boundary causes significant vorticity on both sides of the post. The meniscus at the film edge is shown as gray and the glass film holder as blue.

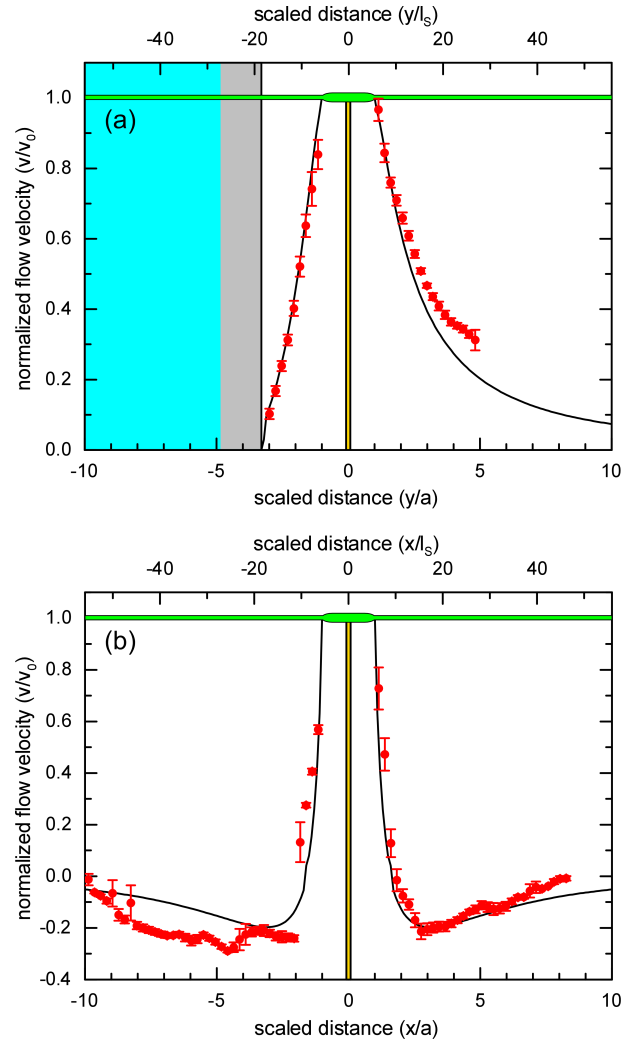


FIG. 9. (Color online) Normalized film flow velocity profiles near the inclusion moving perpendicular to the film boundary shown in Fig. 8, measured (a) along y and (b) along x . The black curves are LM model predictions for a disk-like inclusion. Negative velocities indicate flow with a component opposite the post motion.

VI. APPENDIX A: VELOCIMETRIC METHOD

Estimating a velocity field from an image sequence is a very general problem in computer vision that is directly applicable to many fields of research. The general concept of the technique applied here [29] is to use a block-matching algorithm to find the displacement vector that minimizes the difference between the same subsections of consecutive images for a specified error functional. In this manner, a two-dimensional velocity field may be obtained for each image in the sequence.

For a given image sequence $I(x, y, t)$, the algorithm begins by segmenting the first image into k subsections (tiles) positioned at (X_k, Y_k) . Then, for each tile in the image a two-dimensional search is performed that seeks to minimize the function

$$F_{\text{err}} = F_{\text{ID}} + \lambda F_{\text{S}}, \quad (\text{A1})$$

where F_{ID} is the absolute intensity difference between image subdivisions, F_{S} represents a velocity field smoothness constraint, and λ is a free parameter that sets the relative weighting between the two functions. The intensity difference contribution for the k th tile is

$$F_{\text{ID}} = \int_{\text{tile}} |I(X_k, Y_k, t) - I(X_k + \Delta x, Y_k + \Delta y, t + \Delta t)| dx dy, \quad (\text{A2})$$

where Δx and Δy are the components of the displacement vector \mathbf{d} , Δt is the time between frames, and the integral is over the tile area. The smoothness contribution is

$$F_{\text{S}} = 1 - \exp(-\tau c_s^2), \quad (\text{A3})$$

where

$$c_s = \sqrt{\left(\frac{dv_x}{dx}\right)^2 + \left(\frac{dv_x}{dy}\right)^2 + \left(\frac{dv_y}{dx}\right)^2 + \left(\frac{dv_y}{dy}\right)^2},$$

and the velocity derivatives are calculated at (X_k, Y_k) . The velocity derivative tolerance is set by the free parameter τ . Typically, the values of λ and τ are chosen such that F_{S} is comparable to twice the standard deviation of $I(x, y, t)$ multiplied by the tile area when c_s^2 exceeds the tolerance $1/\tau$. The displacement vector \mathbf{d} that minimizes the combined error yields a velocity estimate for tile k of $\mathbf{v}(X_k, Y_k, t) = \mathbf{d}/\Delta t$. This minimization process is repeated for each tile and each image to yield a velocity field $\mathbf{v}(x, y, t)$.

The choice of error functional described above carries with it a number of consequences. First, the use of the absolute intensity difference effectively assumes that, to a good approximation, brightness is conserved between

frames. Second, by imposing a smoothness constraint on the velocity field, it is assumed that the actual flow field does not have velocity gradients that exceed $\sim 1/\sqrt{\tau}$. In practice it is found that imposing a soft penalty on the smoothness of the velocity field allows for some abrupt variation, but the occurrence of unphysical or spurious vectors is reduced. Finally, the smoothness constraint requires knowledge of the local velocity field in the neighborhood of the k th tile. An initial guess for the velocity field may be provided in any number of ways, but, fundamentally, accurate velocity information is not known prior to the error minimization process. To resolve this issue, an iterative, multi-resolution technique is employed to estimate the velocity field, where the first iteration carries out the minimization process using only the intensity difference component. Full details of the method and tests of its performance may be found in [30].

In this way, a two-dimensional velocity field is obtained for each frame in the image sequence at a specified final resolution that is some fraction of the original image resolution.

VII. APPENDIX B: CALCULATION OF VELOCITY PROFILES IN AIR

To model the air flow induced by a long, thin oscillating post moving in the transverse direction, we consider a coaxial system comprising a solid cylinder of radius b (representing the post) embedded in a cylindrical chamber of radius R (representing the film holder). A general solution of the flow field in this geometry may be derived following Happel and Brenner [31]. Assuming that the post is moving at speed v_0 , the flow velocities in the radial and tangential directions are given by

$$v_r = \frac{1}{r} \frac{\partial \Psi}{\partial \theta}, \quad v_\theta = -\frac{\partial \Psi}{\partial r}, \quad (\text{B1})$$

where Ψ is the stream function

$$\Psi = \sin \theta \left[\frac{1}{8} C r^3 + \frac{1}{2} D r \left(\ln r - \frac{1}{2} \right) + E r + \frac{F}{r} \right] \quad (\text{B2})$$

and

$$\begin{aligned} C &= -\frac{8v_0}{2b^2 R^2 \left[\left(\frac{1}{b^2} - \frac{1}{R^2} \right) + \ln \left(\frac{b}{R} \right) \left(\frac{1}{b^2} + \frac{1}{R^2} \right) \right]} \\ D &= \frac{2v_0 \left(\frac{1}{b^2} + \frac{1}{R^2} \right)}{\left(\frac{1}{b^2} - \frac{1}{R^2} \right) + \ln \left(\frac{b}{R} \right) \left(\frac{1}{b^2} + \frac{1}{R^2} \right)} \\ E &= \frac{v_0 \left(\frac{1}{b^2} - \ln R \left(\frac{1}{b^2} + \frac{1}{R^2} \right) \right)}{\left(\frac{1}{b^2} - \frac{1}{R^2} \right) + \ln \left(\frac{b}{R} \right) \left(\frac{1}{b^2} + \frac{1}{R^2} \right)} \\ F &= \frac{v_0}{2 \left[\left(\frac{1}{b^2} - \frac{1}{R^2} \right) + \ln \left(\frac{b}{R} \right) \left(\frac{1}{b^2} + \frac{1}{R^2} \right) \right]} \end{aligned}$$

-
- [1] M. L. Henle and A. J. Levine, Phys. Rev. E **81**, 011905 (2010).
 - [2] P. J. R. Spooner, H. E. Friesen, J. Knol, B. Poolman, and A. Watts, Biophys. J. **79**, 756 (2000).
 - [3] S. L. Veatch and S. L. Keller, Phys. Rev. Lett. **94**, 148101 (2005).
 - [4] K. Simons and E. Ikonen, Nature **387**, 569 (1997).
 - [5] R. A. Cone, Nature New Biol. **236**, 39 (1972).
 - [6] M. Poo and R. A. Cone, Nature **247**, 438 (1974).
 - [7] P. G. Saffman and M. Delbrück, Proc. Natl. Acad. Sci. USA **72**, 3111 (1975).
 - [8] P. G. Saffman, J. Fluid Mechanics **73**, 593 (1976).
 - [9] N. Oppenheimer and H. Diamant, Phys. Rev. Lett. **107**, 258102 (2011).
 - [10] J. R. Heringa, F. W. Wiegels, and F. P. H. van Beckum, Physica A: Theoretical and Statistical Physics **108**, 598 (1981).
 - [11] F. W. Wiegels and J. R. Heringa, Canadian Journal of Physics **63**, 44 (1985).
 - [12] B. D. Hughes, B. A. Pailthorpe, and L. R. White, Journal of Fluid Mechanics **110**, 349 (1981).
 - [13] C. Cheung, Y. H. Hwang, X.-l. Wu, and H. J. Choi, Phys. Rev. Lett. **76**, 2531 (1996).
 - [14] P. Cicuta, S. L. Keller, and S. L. Veatch, J. Phys. Chem. B Lett. **111**, 3328 (2007).
 - [15] Z. H. Nguyen, M. Atkinson, C. S. Park, J. MacLennan, M. Glaser, and N. Clark, Phys. Rev. Lett. **105**, 268304 (2010).
 - [16] C. Young, R. Pindak, N. Clark, and R. Meyer, Phys. Rev. Lett. **40**, 773 (1978).
 - [17] A. Eremin, S. Baumgarten, K. Harth, R. Stannarius, Z. H. Nguyen, A. Goldfain, C. S. Park, J. E. MacLennan, M. A. Glaser, and N. A. Clark, Phys. Rev. Lett. **107**, 268301 (2011).
 - [18] A. Pattanaporkratana, C. S. Park, J. E. MacLennan, and N. A. Clark, Ferroelectrics **310**, 275 (2004).
 - [19] A. Pattanaporkratana, C. S. Park, J. E. MacLennan, and N. A. Clark, Ferroelectrics **344**, 71 (2006).
 - [20] F. Schneider, Phys. Rev. E **74**, 021709 (2006).
 - [21] D. Davidov, C. R. Safinya, M. Kaplan, S. S. Dana, R. Schaetzling, R. J. Birgeneau, and J. D. Litster, Phys. Rev. B **19**, 1657 (1979).
 - [22] C. Rosenblatt and N. M. Amer, Appl. Phys. Lett. **36**, 432 (1980).
 - [23] R. C. Weast, *Handbook of Chemistry and Physics* (CRC Press, Cleveland, 1973-1974), 54th ed.
 - [24] A. J. Levine and F. C. MacKintosh, Phys. Rev. E **66**, 061606 (2002).
 - [25] Z. Qi, Z. H. Nguyen, C. S. Park, M. A. Glaser, J. E. MacLennan, N. A. Clark, T. Kuriabova, and T. R. Powers, Phys. Rev. Lett. **113**, 128304 (2014).
 - [26] T. Kuriabova, T. R. Powers, Z. Qi, A. Goldfain, C. S. Park, M. A. Glaser, J. E. MacLennan, and N. A. Clark, Phys. Rev. E **94**, 052701 (2016), URL <http://link.aps.org/doi/10.1103/PhysRevE.94.052701>.
 - [27] V. Prasad, S. A. Koehler, and E. R. Weeks, Phys. Rev. Lett. **97**, 176001 (2006).
 - [28] Z. Qi, C. S. Park, M. A. Glaser, J. E. MacLennan, and N. A. Clark, Phys. Rev. E **93**, 012706 (2016), URL <http://link.aps.org/doi/10.1103/PhysRevE.93.012706>.
 - [29] R. P. Wildes, M. J. Amabile, A. Lanzillotto, and T. Leu, Computer Vision and Image Understanding **80**, 246 (2000).
 - [30] T. Munsat and S. J. Zweben, Rev. Sci. Instrum. **77**, 103501 (2006).
 - [31] J. Happel and H. Brenner, *Low Reynolds number hydrodynamics: with special applications to particulate media*, vol. 1 (Springer Science & Business Media, 1983).